Nano-Micro Letters
e-ISSN 2150-5551
CN 31-2103/TB
ARTICLE
https://doi.org/10.1007/s40820-025-01934-7

Cite as
Nano-Micro Lett.
(2026) 18:78

Received: 6 June 2025
Accepted: 3 September 2025


# Solid–State Hydrogen Storage Materials with Excellent Selective Hydrogen Adsorption in the Presence of Alkanes, Oxygen, and Carbon Dioxide by Atomic Layer Amorphous $Al_2O_3$ Encapsulation

Fanqi Bu[1], Zhenyu Wang[1] ✉, Ali Wajid[2], Rui Zhai[1], Ting Liu[3], Yaohua Li[1], Xin Ji[1], Xin Liu[1], Shujiang Ding[2], Yonghong Cheng[1], Jinying Zhang[1] ✉

## HIGHLIGHTS

- Gas selective amorphous $Al_2O_3$ encapsulation was constructed on highly reactive $MgH_2$ using atomic layer deposition.
- Hydrogen selective adsorption was achieved in the impure hydrogen atmosphere containing impurities ($O_2$, $N_2$, $CH_4$, and $CO_2$).
- Excellent air stability with no MgO or $Mg(OH)_2$ generated after 3 months of air exposure was achieved.

**ABSTRACT** Metal hydrides with high hydrogen density provide promising hydrogen storage paths for hydrogen transportation. However, the requirement of highly pure $H_2$ for re-hydrogenation limits its wide application. Here, amorphous $Al_2O_3$ shells (10 nm) were deposited on the surface of highly active hydrogen storage material particles ($MgH_2$–ZrTi) by atomic layer deposition to obtain $MgH_2$–ZrTi@$Al_2O_3$, which have been demonstrated to be air stable with selective adsorption of $H_2$ under a hydrogen atmosphere with different impurities ($CH_4$, $O_2$, $N_2$, and $CO_2$). About 4.79 wt% $H_2$ was adsorbed by $MgH_2$–ZrTi@10nm$Al_2O_3$ at 75 °C under 10%$CH_4$ + 90%$H_2$ atmosphere within 3 h with no kinetic or density decay after 5 cycles (~ 100% capacity retention). Furthermore, about 4 wt% of $H_2$ was absorbed by $MgH_2$–ZrTi@10nm$Al_2O_3$ under 0.1%$O_2$ + 0.4%$N_2$ + 99.5%$H_2$ and 0.1%$CO_2$ + 0.4%$N_2$ + 99.5%$H_2$ atmospheres at 100 °C within 0.5 h, respectively, demonstrating the selective hydrogen absorption of $MgH_2$–ZrTi@10nm$Al_2O_3$ in both oxygen-containing and carbon dioxide-containing atmospheres hydrogen atmosphere. The absorption and desorption curves of $MgH_2$–ZrTi@10nm$Al_2O_3$ with and without absorption in pure hydrogen and then in 21%$O_2$ + 79%$N_2$ for 1 h were found to overlap, further confirming the successful shielding effect of $Al_2O_3$ shells against $O_2$ and $N_2$. The $MgH_2$–ZrTi@10nm$Al_2O_3$ has been demonstrated to be air stable and have excellent selective hydrogen absorption performance under the atmosphere with $CH_4$, $O_2$, $N_2$, and $CO_2$.

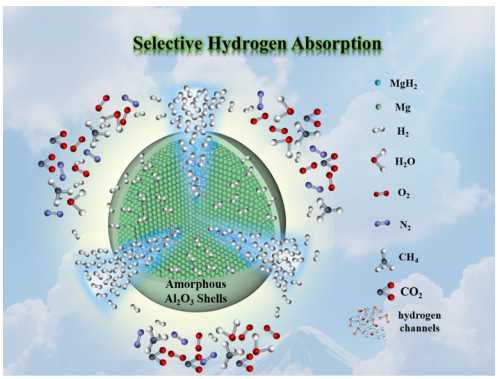


**KEYWORDS** Hydrogen storage; Magnesium hydrides; Selective hydrogen adsorption; Air stability; Amorphous $Al_2O_3$ shells

✉ Zhenyu Wang, z.wang@mpi-susmat.de; Jinying Zhang, jinying.zhang@mail.xjtu.edu.cn
[1] State Key Laboratory of Electrical Insulation and Power Equipment, Center of Nanomaterials for Renewable Energy (CNRE), School of Electrical Engineering, Xi'an Jiaotong University, Xi'an, Shaanxi 710049, People's Republic of China
[2] School of Chemistry, Xi'an Key Laboratory of Sustainable Energy Materials Chemistry, State Key Laboratory for Mechanical Behavior of Materials, Xi'an Jiaotong University, Xi'an 710049, People's Republic of China
[3] Aviation Engineering School, Air Force Engineering University, Xi'an 710038, People's Republic of China

Published online: 24 October 2025

## 1 Introduction

The $H_2$ is expected to play an important role in the future energy system as a clean renewable energy carrier with high energy density [1]. However, the storage and transportation of $H_2$ is still a bottleneck for the application of hydrogen energy. Metal hydrides with high hydrogen density are crucial for hydrogen storage and transportation. However, hydrogenation of metal hydrides with high hydrogen density must be conducted in a pure $H_2$ atmosphere (99.999%) to prevent poisoning [2, 3]. The $MgH_2$ is a typical metal hydride with high hydrogen storage density, which was demonstrated to provide a high theoretical gravimetric (~7.6 wt% $H_2$) as well as volumetric (~110 kg $m^{-3}$ $H_2$) hydrogen storage density. However, the application of $MgH_2$ is still limited to high dehydrogenation temperature, slow kinetics, and degrading cycling performance, especially the requirement of high pure $H_2$ for hydrogenation due to its high reactivity. Various modifications including alloying [4, 5], nanosizing [6–9], and catalysts [2, 3, 10, 11] have been tried to enhance the kinetic properties of $MgH_2$. The catalysts, especially transition metal-based catalysts (Ti, Zr, etc.) with 3*d* or 4*d* electronic orbitals, have been demonstrated to significantly enhance the kinetic of $MgH_2$ [2, 10, 12–14]. Highly efficient reversible hydrogen storage in magnesium-based composites has been achieved through solar radiation under effective catalyst modification [15–17]. However, the stability of $MgH_2$/Mg under different atmospheres has only been reported in very few studies in the form of air stability [18–20]. Nevertheless, the selective hydrogen absorption by hydrogen storage materials with high storage density in complex hydrogen atmospheres has not yet been realized and rarely been attempted.

The polymer encapsulation [19] and carbon layer coating [18, 20] were attempted to solve the air sensitivity of hydrogen storage materials. The Magnesium nanoparticles (~ 5 nm) were synthesized in poly(methyl methacrylate) (PMMA) matrix to enhance their air stability by a liquid-phase reaction method to release 4.64 wt% $H_2$ [19], where a small amount of MgO and $Mg(OH)_2$ were still detected after air exposure for 3 days. The Mg nanoparticles were also tried to be coated by carbon shells by a methane plasma metal reaction method to achieve extremely high air stability [18], where no MgO was detected after being exposed to air for 3 months. However, the dehydrogenation temperature and kinetic were found to be unsatisfactory, with 5 wt% of $H_2$ released from Mg@C at 350 °C for 20 min. The $MgH_2$ particles were also encapsulated in graphene nanorods by a wet chemical reduction method to achieve high air-stability [20], while about 5.3 wt% of $H_2$ was observed to be released at 300 °C for 45 min. Bulk magnesium-nickel-based hydride through water treatment to enhance its air stability [5], while a hydrogen storage density of 3.5 wt% was obtained due to the weight of Ni [5, 21]. The air stability of Mg/$MgH_2$ has been demonstrated to be enhanced to some extent with sacrifice of dehydrogenation kinetic and density. Various transition metal-based catalysts (such as Zr and Ti) have been demonstrated to effectively improve the dehydrogenation kinetics of hydrogen storage materials [2, 3, 6, 9, 21], which could be adopted to enhance the hydrogen storage performance of $MgH_2$.

Most importantly, the hydrogenation of magnesium-based composites must be performed under a pure $H_2$ atmosphere to prevent the poisoning of hydrogen storage materials [2, 3, 7, 8, 22]. The selective storage of hydrogen in a complex atmosphere is extremely important for the wide application of hydrogen storage materials, which could even be directly applied to industrial by-product hydrogen [23]. Alkanes are one of the main impurities in by-product hydrogen, where 24–28% $CH_4$ is included in coke oven gas [24]. However, the $CH_4$ was found to react with $MgH_2$ even under 1.0 bar $CH_4$ to significantly reduce the hydrogen storage performance of $MgH_2$ [25]. The other impurities (such as oxygen or water) are more reactive with $MgH_2$ [19, 20], which was usually avoided for hydrogen storage materials.

Here, we report a method to encapsulate $MgH_2$ particles with homogeneously distributed hydrogen channels ($MgH_2$–ZrTi) by atomic layers of amorphous $Al_2O_3$ shells through atomic layer deposition (ALD) to obtain $MgH_2$–ZrTi@$Al_2O_3$. The amorphous $Al_2O_3$ shells were found to be inert, effectively shielding against $H_2O$, $O_2$, $N_2$, $CH_4$, and $CO_2$, while allowing $H_2$ to penetrate easily. The selective hydrogen absorption of $MgH_2$–ZrTi@10nm$Al_2O_3$ has been demonstrated under hydrogen atmospheres with 10% $CH_4$, 0.1% $CO_2$, and varying contents of $O_2$ and $N_2$.

 https://doi.org/10.1007/s40820-025-01934-7

## 2 Experimental Details

### 2.1 Preparation of $MgH_2$–ZrTi@$Al_2O_3$ and Mg–ZrTi@$Al_2O_3$

The commercial $MgH_2$ (MG power Corp) was first coated with 10 nm $ZrO_2$ by ALD, ball milled with few layers $Ti_3C_2$ (FL–$Ti_3C_2$) with the weight ratio of 19:1 to obtain $MgH_2$–ZrTi according to our reported work [26]. The as-produced $MgH_2$–ZrTi was then coated by amorphous $Al_2O_3$ by ALD. Specifically, 0.25 g of $MgH_2$–ZrTi powder was placed in a glass vial containing 10 mL of anhydrous cyclohexane in the glove box and sealed using parafilm. The glass vial containing the mixture was sonicated for 30 min under ice bath, then subsequently added dropwise to a silicon wafer which was heated to 100 °C in the glove box. After the cyclohexane on the wafers was completely evaporated, the wafers with $MgH_2$–ZrTi attached were placed in custom-made steel containers and quickly transferred to the deposition chamber of the ALD system. The ALD process was carried out cyclically, with an average $Al_2O_3$ deposition thickness of 0.1 nm for a single ALD cycle. The single ALD deposition process for $Al_2O_3$ was as follows: An trimethylaluminum (TMA) pulse for 30 ms, followed by an $N_2$ purge for 1.97 s. And an oxygen plasma pulse for 5 s followed by an $N_2$ purge for 1 s. The resulting samples were named $MgH_2$–ZrTi@5nm$Al_2O_3$, $MgH_2$–ZrTi@10nm$Al_2O_3$, and $MgH_2$–ZrTi@20nm$Al_2O_3$, respectively, based on the deposited thickness of $Al_2O_3$. The $MgH_2$–ZrTi after dehydrogenation at 300 °C was coated with 10 nm $Al_2O_3$ by ALD to prepare Mg–ZrTi@10nm$Al_2O_3$ in non-hydrogen state.

### 2.2 Air Stability Tests of $MgH_2$–ZrTi@$Al_2O_3$

The $MgH_2$–ZrTi@$Al_2O_3$ samples obtained from ALD deposition were directly exposed to air, and the exposure times were set to 1 day, 1 week, 1 month, 2 months, and 3 months, respectively. The average temperature was 15 °C and the average humidity was 25% RH.

### 2.3 Hydrogen Selective Adsorption Tests of $MgH_2$–ZrTi@$Al_2O_3$

Hydrogen selective adsorption tests were performed in $10\%CH_4 + 90\%H_2$ and $0.1\%O_2 + 0.4\%N_2 + 99.5\%H_2$ atmosphere at different temperatures. The $0.1\%O_2 + 0.4\%N_2 + 99.5\%H_2$ mixture was obtained by injecting $H_2$ into a vessel containing 0.1 bar of standard air ($21\%O_2 + 79\%N_2$) until the pressure in the vessel reached 21 bar. The $0.1\%CO_2 + 0.4\%N_2 + 99.5\%H_2$ mixture was obtained by injecting $H_2$ into a vessel containing 0.1 bar of $21\%CO_2 + 79\%N_2$ until the pressure in the vessel reached 21 bar. The high concentration of $O_2$ was performed using a two-step method for hydrogenation, where the sample was first heated under pure hydrogen and followed by $21\%O_2 + 79\%N_2$ at 75 °C for 1 h.

## 3 Results and Discussion

### 3.1 Structure Characterization of $MgH_2$–ZrTi@$Al_2O_3$

The $MgH_2$–ZrTi with low reaction temperature, fast kinetics as well as stable cycling properties were prepared by introducing oxygen-rich vacancies of Zr, Ti components to $MgH_2$ in our previous study [26]. Amorphous $Al_2O_3$ shells were constructed on $MgH_2$–ZrTi particles by ALD to achieve selective hydrogen absorption at moderate temperatures (75–100 °C). The as-produced $MgH_2$–ZrTi particles were observed by SEM to have irregular shapes (Fig. 1a) [26], with about 90% of the particles distributed in the range of 100–500 nm and a very small fraction up to 1 μm (Fig. S1a). No detectable variation was observed in the morphology or size distribution after the deposition of amorphous $Al_2O_3$ ($MgH_2$–ZrTi@10nm$Al_2O_3$, Fig. 1b), indicating no melting or growth of $MgH_2$ particles during the ALD process. Furthermore, no difference was observed in the X-ray diffraction (XRD) patterns of $MgH_2$–ZrTi before and after the coating of amorphous $Al_2O_3$ (Fig. 1c). Only diffraction peaks at 27.9°, 35.7°, 39.9°, 54.6°, and 68.8°, corresponding to the (110), (101), (200), (211), and (112) planes of $MgH_2$, were detected from the XRD patterns of $MgH_2$–ZrTi and $MgH_2$–ZrTi@10nm$Al_2O_3$ (Fig. 1c, ♥). No dehydrogenation or oxidation product was detected from the XRD of

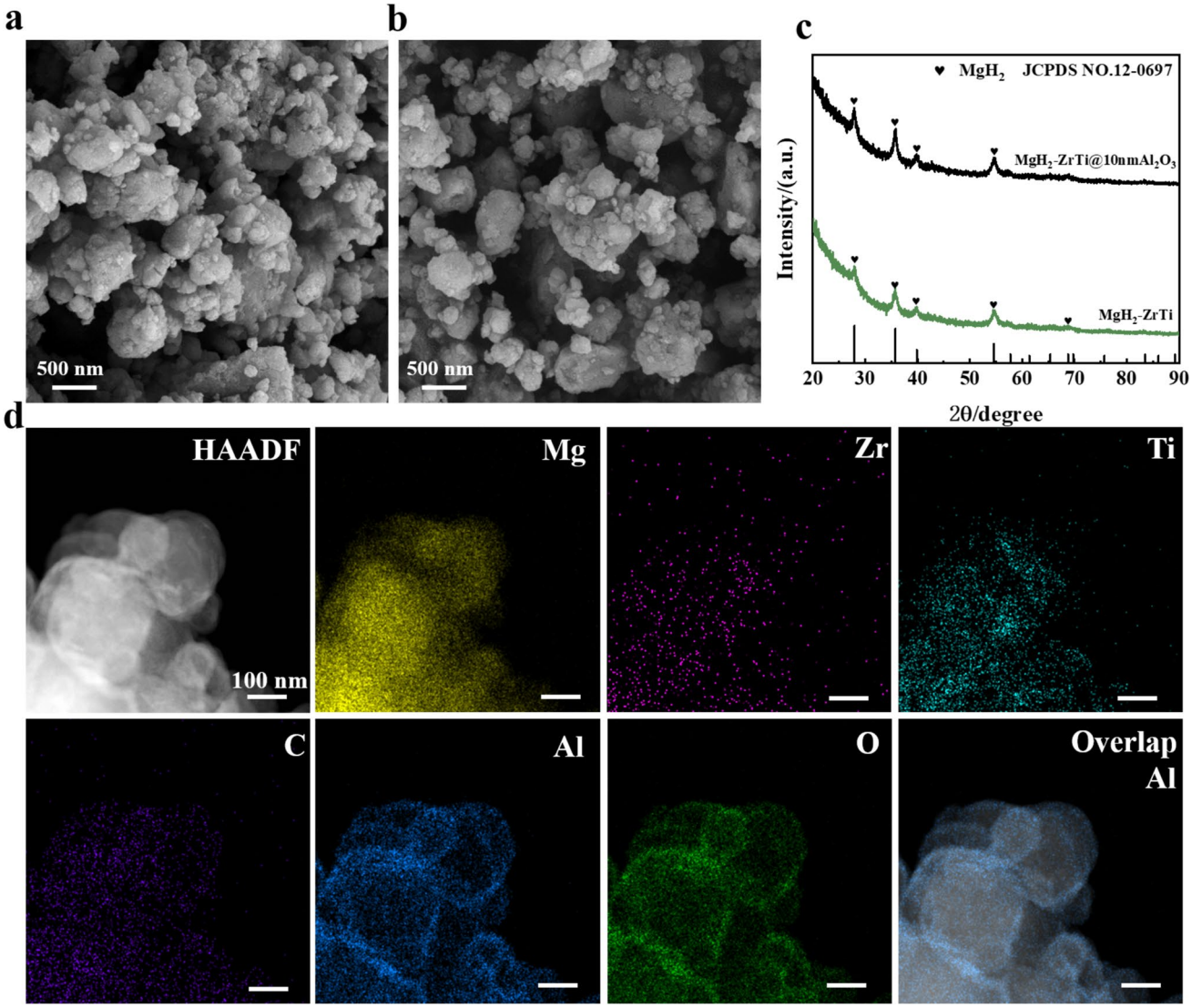


**Fig. 1** Characterization of $MgH_2$–ZrTi and $MgH_2$–ZrTi@10nm$Al_2O_3$. SEM image of **a** $MgH_2$–ZrTi and **b** $MgH_2$–ZrTi@10nm$Al_2O_3$. **c** XRD spectra of $MgH_2$–ZrTi (green) and $MgH_2$–ZrTi@10nm$Al_2O_3$ (black). **d** HAADF-STEM and elemental mapping analysis of $MgH_2$–ZrTi@10nm$Al_2O_3$

$MgH_2$–ZrTi@10nm$Al_2O_3$, further confirmed no negative reaction occurred during ALD processing for hydrogen storage materials. No diffraction peak of $Al_2O_3$ was observed from $MgH_2$–ZrTi@10nm$Al_2O_3$, suggesting the amorphous features of $Al_2O_3$ from the ALD process. This situation is consistent well with reported metal oxides prepared by ALD [27, 28], where no XRD signal of deposited metal oxides was detected. Only interplanar spacings of 0.25 nm corresponding to the (101) planes of $MgH_2$ (JCPDS No. 12-0697) were observed from the HRTEM images of $MgH_2$–ZrTi@10nm$Al_2O_3$ (Fig. S2), consistent well with XRD results. The successful coating of $Al_2O_3$ shells was clearly observed by HAADF-STEM with corresponding elemental analyses on $MgH_2$–ZrTi@10nm$Al_2O_3$ (Fig. 1d). The Al and O elements were observed to be clearly distributed as thin atomic layers on the surface of $MgH_2$ particles, where Zr, Ti, and C were detected to be homogeneously distributed inside $MgH_2$ particles as hydrogen channels [26].

 https://doi.org/10.1007/s40820-025-01934-7

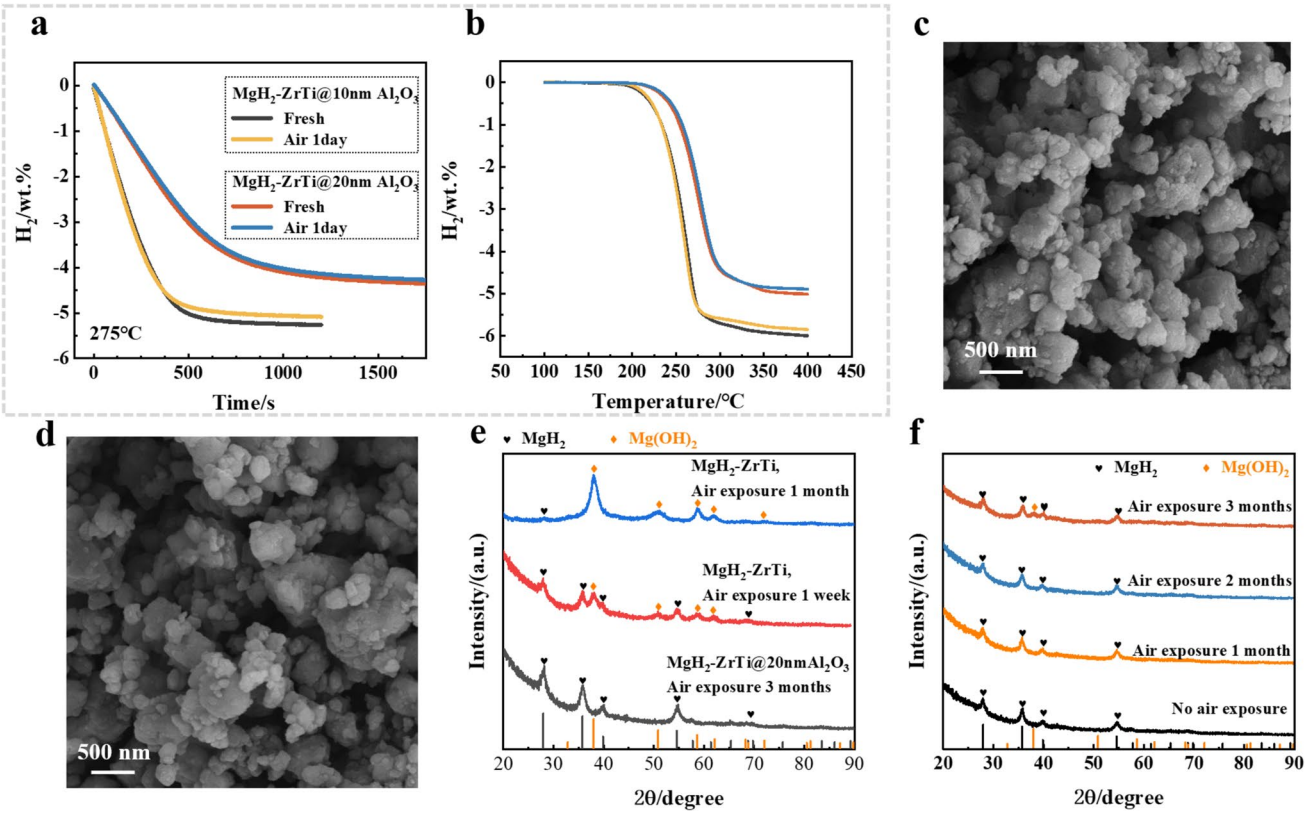


**Fig. 2** **a** Isothermal dehydrogenation (275 °C) and **b** TPD curves of $MgH_2$–ZrTi@10nm$Al_2O_3$ (fresh–black, exposure to air for 1 day–yellow) and $MgH_2$–ZrTi@20nm$Al_2O_3$ (fresh–red, exposure to air for 1 day–blue) before and after exposure to air for 1 day. SEM images of $MgH_2$–ZrTi@10nm$Al_2O_3$ after exposure to air for **c** 1 month and **d** 2 months. XRD spectra of **e** $MgH_2$–ZrTi, $MgH_2$–ZrTi@20nm$Al_2O_3$, and **f** $MgH_2$–ZrTi@10nm$Al_2O_3$ before and after air exposure for different times

### 3.2 Shied Effect of Amorphous $Al_2O_3$ Coating on $MgH_2$–ZrTi

The isothermal (Fig. 2a) and temperature programmed dehydrogenation (TPD, Fig. 2b) properties of $MgH_2$–ZrTi@10nm$Al_2O_3$ and $MgH_2$–ZrTi@20nm$Al_2O_3$ before and after exposure to air were measured to reveal the shielding effect of amorphous $Al_2O_3$ shells to $H_2O$ and $O_2$. The dehydrogenation performance of $MgH_2$–ZrTi was found to deteriorate significantly after exposure to air for 1 day (Fig. S3). Only 0.036 wt% of $H_2$ was detected to be released from $MgH_2$–ZrTi after exposure to air for 1 day at 275 °C in 20 min, while 6.20 wt% $H_2$ was detected at 275 °C in 6 min from $MgH_2$–ZrTi before exposure to air (Fig. S3a). The dehydrogenation temperature of $MgH_2$–ZrTi was found to be significantly increased after exposure to air for 1 day, where only 1.10 wt% of $H_2$ was released even up to 400 °C compared to 6.40 wt% released up to 300 °C for fresh $MgH_2$–ZrTi from TPD measurements (Fig. S3b). However, no significant variation was detected for the dehydrogenation of $MgH_2$–ZrTi@$Al_2O_3$ (Fig. 2a, b), where less than 0.2 wt% variation was observed for $MgH_2$–ZrTi@$Al_2O_3$ after exposure to air for 1 day. The dehydrogenation curves of $MgH_2$–ZrTi@$Al_2O_3$ before and after air exposure were found to overlap for the isothermal one within 0–400 s (Fig. 2a) as well as TPD one within 100–280 °C (Fig. 2b). About 4.87 wt% of $H_2$ was released at 275 °C within 500 s from $MgH_2$–ZrTi@10nm$Al_2O_3$ after exposure to air for 1 day (Fig. 2a). The hydrogen storage density was found to decrease with increasing $Al_2O_3$ thickness from 10 to 20 nm (Fig. 2a, b). About 4.23/4.31 wt% $H_2$ was released at 275 °C within 25 min for $MgH_2$–ZrTi@20nm$Al_2O_3$ before/after air exposure (Fig. 2a). The dehydrogenation temperature of $MgH_2$–ZrTi@$Al_2O_3$ was also found to increase with increasing $Al_2O_3$ thickness (Fig. 2b). The $ZrO_2$ and $Ti_3C_2$ components of $MgH_2$–ZrTi composites were deduced from

the maximum dehydrogenation capacity of fresh $MgH_2$–ZrTi (6.77 wt%, TPD in Fig. S3b) to have a mass ratio of about 11 wt%.

The XRD features of $Mg(OH)_2$ (JCPDS NO. 07-0239, Fig. 2e, yellow ♦) was clearly detected in addition to XRD features of $MgH_2$ (27.9°(110), 35.7°(101), 39.9°(200), 54.6°(211), and 68.8°(112), Fig. 2e, black ♥) for $MgH_2$–ZrTi after exposure to air, whose intensity was found to increase with increasing exposure time (Fig. 2e from red line to blue line), consistent well with the degradation of its hydrogen storage performance (Fig. S3). In order to estimate $Mg(OH)_2$ impurity quantitatively, the $MgH_2$–ZrTi (100 mg) was heated at 200 °C for 48 h in air after exposure to air for 1 week. The mass of the product was measured to be 181.2 mg. Both $MgH_2$ and $Mg(OH)_2$ (Fig. 2e, red line) was detected in $MgH_2$–ZrTi before heating treatment, while only $Mg(OH)_2$ (Fig. S4) was detected after heating treatment. The $MgH_2$ and $Mg(OH)_2$ in the $MgH_2$–ZrTi after exposure to air for 1 week was estimated to be about 66 and 34 mg, respectively, based on the mass variation. The $Mg(OH)_2$ impurities in $MgH_2$–ZrTi after exposure to air for 1 week was deduced to be about 34%. No $Mg(OH)_2$ was detected from the XRD of $MgH_2$–ZrTi@5nm$Al_2O_3$ after exposure to air for 1 week (Fig. S5), demonstrating that the 5 nm amorphous $Al_2O_3$ encapsulation is also effective in protecting $MgH_2$/Mg particles. However, the $Mg(OH)_2$ features were detected after exposure to air for 1 month and 6 weeks, with its content increasing continuously (Fig. S5). However, only diffraction features of $MgH_2$ were detected for $MgH_2$–ZrTi@10nm$Al_2O_3$ and $MgH_2$–ZrTi@20nm$Al_2O_3$ even after exposure to air for 2 to 3 months (Fig. 2e, f), where no MgO or $Mg(OH)_2$ was detected. Only tiny diffraction peaks of $Mg(OH)_2$ were detected from $MgH_2$–ZrTi@10nm$Al_2O_3$ after exposure to air for 3 months (Fig. 2f, red line). No morphological changes were observed on the surface of $MgH_2$–ZrTi@10nm$Al_2O_3$ particles after exposure to air for 1 month (Fig. 2c) and even 2 months (Fig. 2d). No $Mg(OH)_2$ was detected from $MgH_2$–ZrTi@10nm$Al_2O_3$ after exposure to air for 3 weeks when the air condition was adjusted from 15 °C to 25% RH to 30 °C and 50% RH (Fig. S6), further confirmed the air stability of the $MgH_2$–ZrTi@10nm$Al_2O_3$. No diffraction peaks of MgO and $Mg(OH)_2$ was detected from the Mg–ZrTi@10nm$Al_2O_3$ in non-hydrogen state after exposure to air for 3 weeks (Fig. S7) either, demonstrating an excellent protection effect of 10 nm amorphous $Al_2O_3$ shells for the hydrogen storage particles. The $MgH_2$–ZrTi@5nm$Al_2O_3$, $MgH_2$–ZrTi@10nm$Al_2O_3$ and $MgH_2$–ZrTi@20nm$Al_2O_3$ have been demonstrated to maintain intact without obvious oxidation after exposure to air for 1 week, 2 months and 3 months, respectively. The 10 nm $Al_2O_3$ coating has been demonstrated to be effective enough to prevent the degradation of $MgH_2$–ZrTi from exposure to air ($H_2O$ and $O_2$).

### 3.3 Hydrogen Selective Adsorption of $MgH_2$–ZrTi@10nm$Al_2O_3$ in the Presence of $CH_4$, $O_2$, $N_2$ and $CO_2$ Impurities

The selective absorption of $MgH_2$–ZrTi@10nm$Al_2O_3$ was first explored under a hydrogen atmosphere in the presence of 10% methane (10 vol%$CH_4$ + 90 vol%$H_2$). About 4.79 wt% $H_2$ was detected to be adsorbed by $MgH_2$–ZrTi@10nm$Al_2O_3$ under 10%$CH_4$ + 90%$H_2$ (30 bar), slightly less than that (5.00 wt%) under pure $H_2$ (30 bar, 99.999%) at 75 °C in 3 h (Fig. 3a). The absorption densities under two different atmospheres were observed to converge with increasing absorption time (Fig. 3a). The slightly slower hydrogenation kinetic under an impure hydrogen atmosphere than that under a pure hydrogen atmosphere was attributed to lower real-time hydrogen pressure of the impure atmosphere than that of pure one during the hydrogenation process, which is confirmed by the overlap of the hydrogenation curve of $MgH_2$–ZrTi@10nm$Al_2O_3$ under 30 bar pure hydrogen and 35 bar 10%$CH_4$ + 90%$H_2$ (Fig. S8). Strong $MgH_2$ feature (Fig. S9, black line, black ♥) with very weak Mg feature (Fig. S9, black line, orange *) were detected from hydrogenated $MgH_2$–ZrTi@10nm$Al_2O_3$ under impure hydrogen atmosphere (10%$CH_4$ + 90%$H_2$), consistent well with its hydrogenation results (Fig. 3a, yellow). Only a slight difference, slower hydrogenation kinetics, has been demonstrated for $MgH_2$–ZrTi@10nm$Al_2O_3$ under an impure hydrogen atmosphere (10%$CH_4$ + 90%$H_2$) compared to that under a pure hydrogen atmosphere (99.999%). However, the $MgH_2$–ZrTi without $Al_2O_3$ shells was detected to have a much lower absorption density under 10%$CH_4$ + 90%$H_2$ than that under a pure hydrogen atmosphere (Fig. S10). About 4.71 wt% $H_2$ was adsorbed by $MgH_2$–ZrTi in 1 h under pure $H_2$ atmosphere (Fig. S10, green line), whereas about 3.91 wt% was absorbed under 10%$CH_4$ + 90%$H_2$ atmosphere (Fig. S10, blue line). The adsorption capacity of $MgH_2$–ZrTi in 10%$CH_4$ + 90%$H_2$ atmosphere was detected to decay

 https://doi.org/10.1007/s40820-025-01934-7

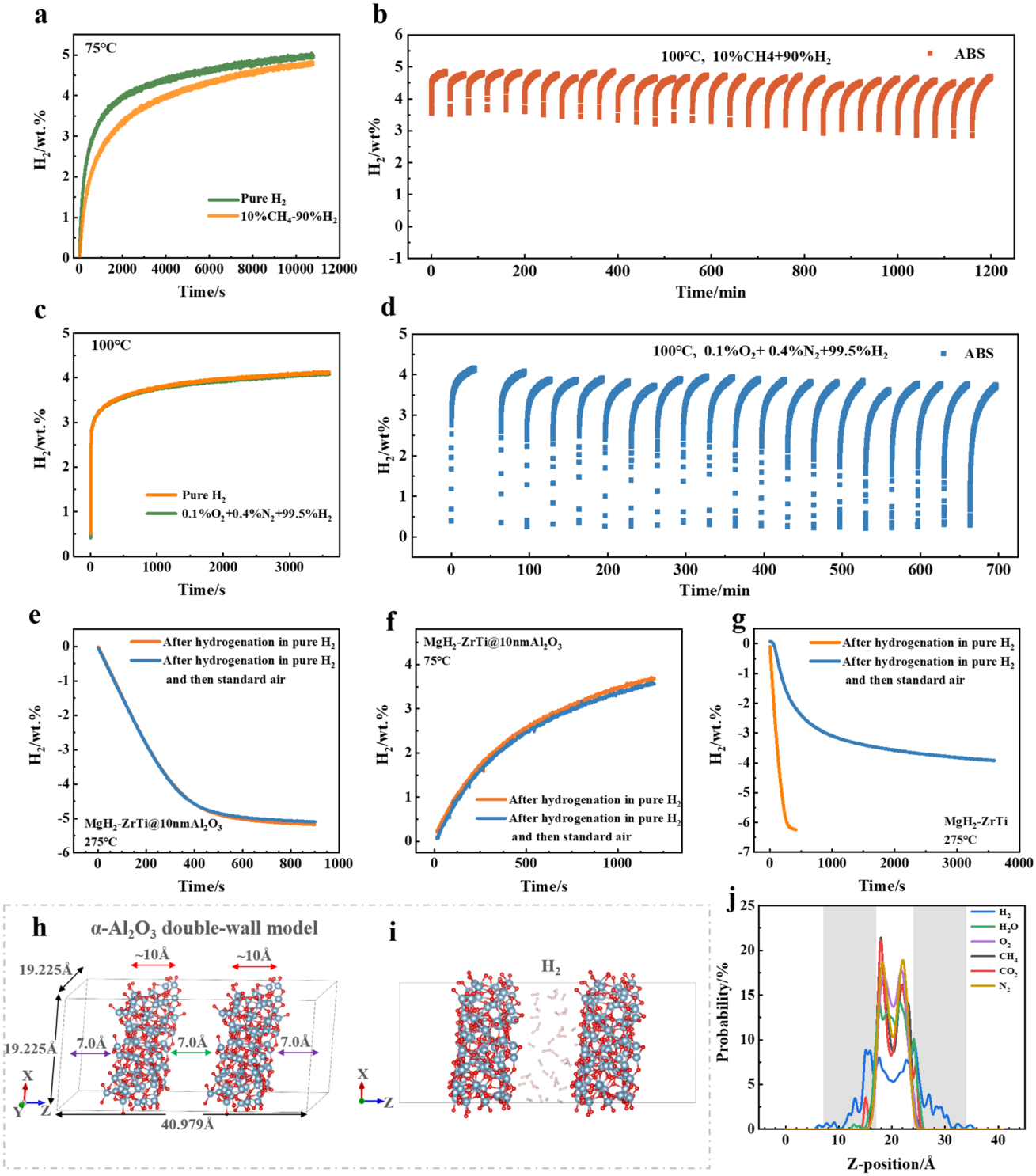


**Fig. 3** Isothermal adsorption curves of **a** $MgH_2$–ZrTi@10nm$Al_2O_3$ at 75 °C in pure $H_2$ and 10%$CH_4$ + 90%$H_2$ atmospheres (30 bar). **b** Isothermal cyclic adsorption curves of $MgH_2$–ZrTi@10nm$Al_2O_3$ at 100 °C under 10%$CH_4$ + 90%$H_2$ atmosphere. **c** Isothermal adsorption curves of $MgH_2$–ZrTi@10nm$Al_2O_3$ in pure $H_2$ and 0.1%$O_2$ + 0.4%$N_2$ + 99.5%$H_2$ atmospheres (16 bar, 100 °C). **d** Isothermal cyclic adsorption curves of $MgH_2$–ZrTi@10nm$Al_2O_3$ at 100 °C under 0.1%$O_2$ + 0.4%$N_2$ + 99.5%$H_2$ atmosphere. Isothermal **e** dehydrogenation and **f** re-hydrogenation curves of $MgH_2$–ZrTi@10nm$Al_2O_3$ after hydrogenation in pure $H_2$ followed 21%$O_2$ + 79%$N_2$ (blue line) at 75 °C for 1 h compared to that only under pure $H_2$ (orange line). **g** Isothermal dehydrogenation curves (275 °C) of $MgH_2$–ZrTi after hydrogenation in pure $H_2$ (orange line) as well as hydrogenation in pure $H_2$ followed by 21%$O_2$ + 79%$N_2$ (blue line) at 75 °C for 1 h. **h** Double-wall α- $Al_2O_3$ model consisting of two parallel slabs and **i** the simulation of the penetration of $H_2$ molecules between the two $Al_2O_3$ slabs. **j** Proportional distribution of various gas molecules along the z-direction

gradually with increasing cycles, with 3.48 wt% as well as 3.18 wt% adsorbed within 1 h for the 2nd and 3rd cycles, respectively (Fig. S10, orange and red lines). Fish scale-like structures (Fig. S11b), amorphous carbon produced from the reaction of $CH_4$ with $MgH_2$–ZrTi particles [25], were detected to emerge on the surface of $MgH_2$–ZrTi after hydrogenation under $10\%CH_4 + 90\%H_2$ atmosphere. The emergence of carbon was confirmed by HAADF-STEM and its elemental analysis of $MgH_2$–ZrTi before and after hydrogenation under$10\%CH_4 + 90\%H_2$ atmosphere, where the carbon range was enhanced after hydrogenation (inside the yellow circle of Figs. S12 and S13). Only XRD features of $MgH_2$ and Mg were detected from the hydrogenated $MgH_2$–ZrTi ($10\%CH_4 + 90\%H_2$, Fig. S9), indicating the amorphous nature of carbon which is consistent well with reported data [25].

The isothermal adsorption performance of $MgH_2$–ZrTi@10nm$Al_2O_3$ was further measured at different temperatures under $10\%CH_4 + 90\%H_2$ atmosphere (Fig. S14a), where 3.86 wt% $H_2$, 5.33 wt% $H_2$, and 5.85 wt% $H_2$ were absorbed at 75, 100, and 125 °C within 1 h. The $MgH_2$–ZrTi@10nm$Al_2O_3$ was observed to reach the inflection point of the adsorption curve at around 4 min at 100 and 125 °C, with 4.33 and 4.84 wt% $H_2$ absorbed, respectively. No Fish scale-like structures of amorphous carbon were observed on the surface of $MgH_2$–ZrTi@10nm$Al_2O_3$ after hydrogenation at 125 °C under $10\%CH_4 + 90\%H_2$ atmosphere from SEM (Fig. S15). No amorphous carbon produced was further confirmed by HAADF-STEM and corresponding elemental analyses (Fig. S16), where no extra carbon was observed on $Al_2O_3$ shells. The selective hydrogen absorption of $MgH_2$–ZrTi@10nm$Al_2O_3$ was further confirmed by its cycling stability under $10\%CH_4 + 90\%H_2$ atmosphere (Figs. S14b and S17). The 1st and 5th adsorption curves of $MgH_2$–ZrTi@10nm$Al_2O_3$ were observed to be almost completely overlapped. About 3.98 and 3.89 wt% $H_2$ was absorbed at 75 °C in 1 h for the 1st and 5th cycle, respectively (Fig. S14b). About 4.86, 4.72, and 4.71 wt% $H_2$ were still absorbed by $MgH_2$–ZrTi@10nm$Al_2O_3$ at 100 °C for 10th, 20th and 30th cycle, with 96.9% capacity retention at the 30th cycle (1st hydrogenation capacity was 4.86 wt%, Fig. 3b). The hydrogenation behavior that did not start from zero is attributable to the excessive rate of hydrogenation during the initial 1–3 s at 100 °C under 30 bar $10\%CH_4 + 90\%H_2$ atmosphere. The $MgH_2$–ZrTi@10nm$Al_2O_3$ has been demonstrated to have excellent selective hydrogenation under an impure hydrogen atmosphere of $10\%CH_4 + 90\%H_2$.

The selective absorption of $MgH_2$–ZrTi@10nm$Al_2O_3$ in the presence of $O_2$ and $N_2$ was also explored with different content. The isothermal re-hydrogenation curve of $MgH_2$–ZrTi@10nm$Al_2O_3$ under $0.1\%O_2 + 0.4\%N_2 + 99.5\%H_2$ (100 °C, 16 bar) was found to overlap with that under pure $H_2$ (Fig. 3c), about 4.10 wt% of $H_2$ was adsorbed at 100 °C within 1 h. However, the isothermal hydrogenation behavior of blank $MgH_2$–ZrTi was observed to attenuate significantly under $0.1\%O_2 + 0.4\%N_2 + 99.5\%H_2$, only 2.51 wt% $H_2$ absorbed at 100 °C within 1 h (Fig. S18, blue line). 3.71 wt% $H_2$ was absorbed by $MgH_2$–ZrTi at 100 °C in 2 min under pure $H_2$ at 100 °C (Fig. S18, green line). The $MgH_2$–ZrTi@10nm$Al_2O_3$ was observed to have rapid hydrogenation at moderate temperatures (75–125 °C) under $0.1\%O_2 + 0.4\%N_2 + 99.5\%H_2$ (Fig. S19a), where 3.15 wt% $H_2$ was absorbed at 75 °C within 1 h and 3.93 wt% $H_2$ was absorbed at 125 °C within 3 min. The three hydrogenation cycle curves of $MgH_2$–ZrTi@10nm$Al_2O_3$ under $0.1\%O_2 + 0.4\%N_2 + 99.5\%H_2$ atmosphere at 100 °C were detected to be almost overlapped (Fig. S19b). However, the cycling performance of $MgH_2$–ZrTi under $0.1\%O_2 + 0.4\%N_2 + 99.5\%H_2$ atmosphere at 100 °C was observed to decrease significantly (Fig. S18), with 2.52, 1.93, and 1.33 wt% of $H_2$ absorbed within 1 h for the 1st, 2nd, and 3rd cycle, respectively. In addition, about 3.94 wt% as well as 3.70 wt% $H_2$ were still absorbed by $MgH_2$–ZrTi@10nm$Al_2O_3$ for the 10th and 20th cycle at 100 °C under $0.1\%O_2 + 0.4\%N_2 + 99.5\%H_2$, with a capacity retention of 89.4% at the 20th cycle (the 1st hydrogenation capacity was 4.14 wt%, Fig. 3d). Small fluctuations in the capacity during the hydrogenation cycles (e.g., 7th and 8th hydrogenation processes, Fig. 3d) were introduced by small sample volume variation during the test [28]. No diffraction peaks of MgO (JCPDS No. 45-0946) were observed in the XRD of $MgH_2$–ZrTi@10nm$Al_2O_3$ (Fig. S20, green line) after hydrogenation under $0.1\%O_2 + 0.4\%N_2 + 99.5\%H_2$, where only $MgH_2$ (JCPDS No. 12-0697, black ♥) and Mg (JCPDS No. 35-0821, orange *) were detected. However, $MgH_2$ (JCPDS No. 12-0697, black ♥), Mg (JCPDS No. 35-0821, orange *) and MgO (JCPDS No. 45-0946, blue Δ) were observed in the XRD pattern of $MgH_2$–ZrTi after hydrogenation under $0.1\%O_2 + 0.4\%N_2 + 99.5\%H_2$ at 100 °C (Fig. S20, gray line). The $Al_2O_3$ shells have been

 https://doi.org/10.1007/s40820-025-01934-7

demonstrated to effectively shield the $MgH_2$/Mg to react with $O_2$ to yield MgO, resulting in excellent selective hydrogen absorption under $0.1\%O_2 + 0.4\%N_2 + 99.5\%H_2$ atmosphere. The $MgH_2$–ZrTi@10nm$Al_2O_3$ has been demonstrated to have excellent hydrogen selective absorption in the presence of $O_2$ and $N_2$.

The selective hydrogen absorption of $MgH_2$–ZrTi@10nm$Al_2O_3$ under high concentration of $O_2$ and $N_2$ was also performed. However, too high concentration of $O_2$ with $H_2$ will cause an explosion during experiments. So selective hydrogen absorption of $MgH_2$–ZrTi@10nm$Al_2O_3$ with a high concentration of $O_2$ was conducted by a two-step method, where the sample was first heated in pure hydrogen and then in $21\%O_2 + 79\%\ N_2$ at 75 °C for 1 h for hydrogenation process. The isothermal re/dehydrogenation curves of $MgH_2$–ZrTi@10nm$Al_2O_3$ after hydrogenation in pure $H_2$ followed by $21\%O_2 + 79\%N_2$ at 75 °C for 1 h were found to overlap with those after hydrogenation in pure $H_2$ (Fig. 3e, f). However, the dehydrogenation curve of $MgH_2$–ZrTi after being treated by pure $H_2$ followed by $21\%O_2 + 79\%N_2$ at 75 °C for 1 h was found to be significantly attenuated than that treated under pure hydrogen (Fig. 3g), only 2.59 wt% of $H_2$ being released in 10 min at 275 °C.

Hydrogen absorption behavior in the presence of $CO_2$ ($0.1\%CO_2 + 0.4\%N_2 + 99.5\%H_2$) was further investigated. Significant attenuation of the hydrogen absorption behavior was observed for the blank $MgH_2$–ZrTi in the presence of $CO_2$ (Fig. S21a). The hydrogen absorption capacity of $MgH_2$–ZrTi in the $H_2$ atmosphere at 100 °C was measured to be 5.25 wt% within 0.5 h (Fig. S21a, green line), while the hydrogen absorption capacities was found to decrease to 1.66 and 0.75 wt% in the first and second cycles under $0.1\%CO_2 + 0.4\%N_2 + 99.5\%H_2$ atmosphere (Fig. S21a, blue and orange lines), respectively. However, the hydrogen absorption curve (Fig. S21b, blue) of $MgH_2$–ZrTi@10nm$Al_2O_3$ under $0.1\%CO_2 + 0.4\%N_2 + 99.5\%H_2$ atmosphere was found to overlap with that under pure $H_2$ (Fig. S21b, green). The hydrogen absorption capacities of $MgH_2$–ZrTi@10nm$Al_2O_3$ under $0.1\%CO_2 + 0.4\%N_2 + 99.5\%H_2$ atmosphere was detected to be 4.05, 4.01, and 3.92 wt% within three cycles (Fig. S21b, blue,orange, and red lines), further confirming the effective protection of amorphous $Al_2O_3$ shells for $MgH_2$/Mg from $CO_2$.

To investigate the penetration behavior of various gases through amorphous $Al_2O_3$ shells, a double-wall α- $Al_2O_3$ model comprising two parallel slabs were constructed (Fig. 3h). The interlayer spacing between the slabs was set to 7 Å, and an additional 14 Å vacuum region was introduced along the z-direction to eliminate image interactions arising from periodic boundary conditions. Amorphous $Al_2O_3$ layers were generated by cleaving an α-$Al_2O_3$ (0001) slab and performing molecular dynamics (MD) simulations at 800 K using a Langevin thermostat within the NVT ensemble for 150 ps [29]. The final configuration was extracted after the system reached thermal equilibrium. Based on HRTEM observations indicating an Al-oxide layer thickness of approximately 10 nm (Fig. S2), a comparable thickness for our model was adopted. To accelerate gas penetration, 40 gas molecules were inserted between the two $Al_2O_3$ slabs for each case (Figs. 3i and S22c-h). The simulations were carried out at 800 K. Due to the elevated gas density, the interlayer spacing tends to expand under pressure. To mitigate this effect, Al and O atoms at the periodic boundaries in the xy-plane were fixed (the gray-shaded region in Fig. S22a). Subsequently, molecular dynamics (MD) simulations were performed for 250 ps using a Langevin thermostat. To monitor gas penetration, we tracked the z-position of representative atoms: H from $H_2$, C from $CO_2$ and $CH_4$, O from $H_2O$ and $O_2$, and N from $N_2$. The penetration behavior was analyzed by plotting histograms of these atomic z-positions (Fig. 3j). The gray-shaded regions in Figs. S22a and 3j represent the spatial extent of the $Al_2O_3$ layer. It is important to note that the surface of the amorphous layer is not atomically flat. The gray region corresponded to the z-position of the outermost atoms of the amorphous $Al_2O_3$ slab. All gases except $H_2$ was found to exhibit narrow probability distributions confined between the $Al_2O_3$ layers or shallowly intercalated near the surface, indicating that only $H_2$ molecules are able to permeate through the amorphous $Al_2O_3$ layer, while other gas species ($O_2$, $H_2O$, $N_2$, $CH_4$, and $CO_2$) are either adsorbed onto or weakly intercalated within the surface region. The MD simulations results are well consistent with reported simulation data [30]. The $H_2$ permeability and selectivity are largely dependent on the size of the nanopore. The $H_2$ permeability was found to increase with increasing pore size, meanwhile hampering the selectivity [30]. Based on the selective hydrogen adsorption behavior of the $MgH_2$–ZrTi@10nm$Al_2O_3$ (Fig. 3a-d) and the results of MD simulations (Fig. 3j), it is inferred that the $Al_2O_3$ shells have a suitable pore size that facilitates the permeation of $H_2$ as well as hinders the permeation of other gases, which

in turn exhibits excellent selective adsorption properties for hydrogen.

### 3.4 Hydrogen Sorption Properties of $MgH_2$–ZrTi@$Al_2O_3$

The hydrogen sorption properties of $MgH_2$ in pure $H_2$ have been demonstrated to be significantly enhanced by the synergistic effect of amorphous $ZrO_2$ as well as Few-layer $Ti_3C_2$ (FL-$Ti_3C_2$) in our previous studies [26]. The effects of the thickness of amorphous $Al_2O_3$ shells on the hydrogen storage performance of $MgH_2$–ZrTi were also explored (Fig. 4a, b). The onset dehydrogenation temperatures of $MgH_2$–ZrTi@5nm$Al_2O_3$ and $MgH_2$–ZrTi@10nm$Al_2O_3$ (Fig. 4a, red and green) were found to be around 185 °C, the same as that of $MgH_2$–ZrTi (Fig. S3b, orange) which is 105 °C lower than that of $MgH_2$ (Fig. 4a, blue) [26]. The TPD curves of $MgH_2$–ZrTi@5nm$Al_2O_3$ and $MgH_2$–ZrTi@10nm$Al_2O_3$ were observed to be almost overlapped between 185 and 275 °C (Fig. 4a).

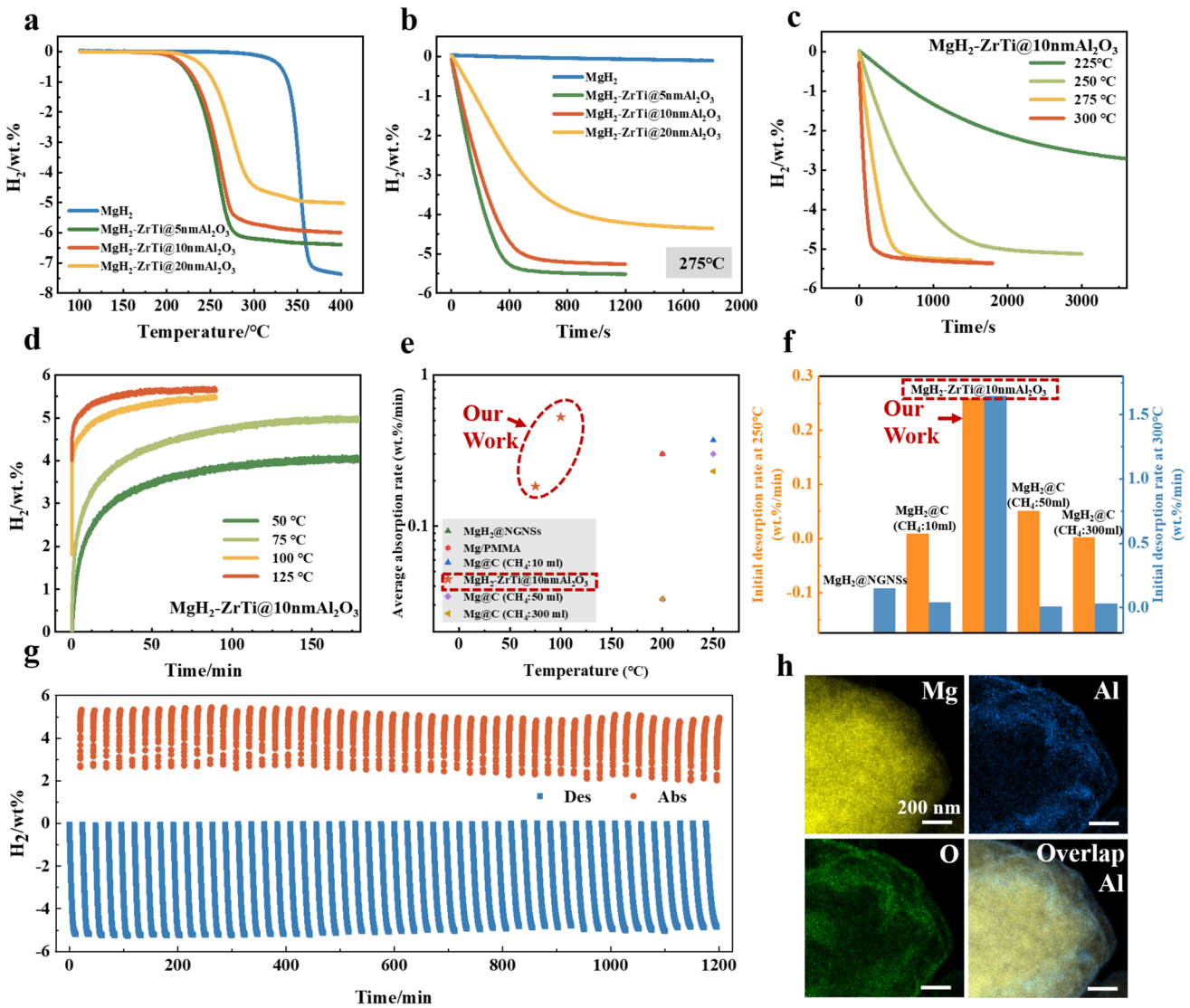


**Fig. 4** **a** TPD and **b** isothermal dehydrogenation (275 °C) of $MgH_2$, $MgH_2$–ZrTi@5nm$Al_2O_3$, $MgH_2$–ZrTi@10nm$Al_2O_3$, and $MgH_2$–ZrTi@20nm$Al_2O_3$. The isothermal **c** dehydrogenation and **d** re-hydrogenation (30 bar $H_2$) of $MgH_2$–ZrTi@10nm$Al_2O_3$ at different temperature. **e** Average re-hydrogenation rates and **f** Initial dehydrogenation rates (250 °C and 300 °C) of $MgH_2$–ZrTi@10nm$Al_2O_3$ compared with reported excellent air-stable Mg-based composites [18–20]. **g** Isothermal dehydrogenation (275 °C/0.05 bar) and re-hydrogenation (275 °C/30 bar $H_2$) cycling curves of $MgH_2$–ZrTi@10nm$Al_2O_3$. **h** EDS elemental mapping analysis of $MgH_2$–ZrTi@10nm$Al_2O_3$ after 50 cycles

 https://doi.org/10.1007/s40820-025-01934-7

However, the maximum dehydrogenation capacity of $MgH_2$–ZrTi@5nm$Al_2O_3$ and $MgH_2$–ZrTi@10 nm $Al_2O_3$ were observed to be 6.39 and 6.00 wt% before 400 °C (Fig. 4a), respectively, due to no hydrogen storage capacity contribution of $Al_2O_3$. The onset dehydrogenation temperature of $MgH_2$–ZrTi@20nm$Al_2O_3$ was detected to increase to 205 °C (Fig. 4a, yellow). Only 4.45 wt% $H_2$ was released from $MgH_2$–ZrTi@20nm$Al_2O_3$ up to 300 °C, which is about 1 wt% less than that of $MgH_2$–ZrTi@10nm$Al_2O_3$. The dehydrogenation kinetics of $MgH_2$–ZrTi@10nm$Al_2O_3$ and $MgH_2$–ZrTi@5nm$Al_2O_3$ (Fig. 4b, red and green) were found to be similar. About 5.02 wt% of $H_2$ was released from $MgH_2$–ZrTi@10nm$Al_2O_3$ at 275 °C within 500 s (Fig. 4b, red). The isothermal dehydrogenation rate of $MgH_2$–ZrTi@20nm$Al_2O_3$ was observed to further slow down significantly (Fig. 4b, yellow), About 4.10 wt% of $H_2$ was released from $MgH_2$–ZrTi@20nm$Al_2O_3$ at 275 °C in 1000 s. The isothermal dehydrogenation of the hydrogen storage materials at 275 °C (Fig. 4b) were normalized based on the theoretical hydrogen storage capacity of $MgH_2$ (7.6 wt%), resulting in normalized hydrogen release curves (Fig. S23). The normalized dehydrogenation curves of $MgH_2$–ZrTi@5nm$Al_2O_3$ and $MgH_2$–ZrTi@10nm$Al_2O_3$ within 200 s were found to almost overlap with dehydrogenation completion within 500 s, while about 1000 s was required for $MgH_2$–ZrTi@20nm$Al_2O_3$ to complete the dehydrogenation process. $MgH_2$–ZrTi@10nm$Al_2O_3$ has been demonstrated to be the best considering kinetics, hydrogen storage density (Fig. 4a, b), and shied effect (Figs. 2 and 3).

The dehydrogenation rates of $MgH_2$–ZrTi@10nm$Al_2O_3$ were observed to be significantly accelerated with increasing temperature from 225 to 300 °C (Fig. 4c). The dehydrogenation of $MgH_2$–ZrTi@10nm$Al_2O_3$ at 250 °C was found to be almost complete within 30 min, releasing about 5 wt% of $H_2$ with an onset dehydrogenation rate (within the first 600 s) of 0.297 wt% $min^{-1}$. About 5.13 wt% was released at 275 °C for 10 min with an onset dehydrogenation rate (within the first 600 s) as high as 0.683 wt% $min^{-1}$. The dehydrogenation curve of $MgH_2$–ZrTi@10nm$Al_2O_3$ was found to reach its inflection point within 3 min at a further increasing temperature to 300 °C, releasing 4.93 wt% of $H_2$. Additionally, $MgH_2$–ZrTi@10nm$Al_2O_3$ were hydrogenated in 30 bar 10%$CH_4$ + 90%$H_2$ and 16 bar 0.1%$O_2$ + 0.4%$N_2$ + 99.5%$H_2$ for 1 h and then heated to the isothermal test temperature (250, 275, and 300 °C) under 2 bar $H_2$ atmosphere for isothermal dehydrogenation tests (Figs. S24a and S25a). The dehydrogenation capacity of $MgH_2$–ZrTi@10nm$Al_2O_3$ after re-hydrogenation in the 10%$CH_4$ + 90%$H_2$ and 0.1%$O_2$ + 0.4%$N_2$ + 99.5%$H_2$ atmospheres was slightly lower than that after re-hydrogenation in the pure $H_2$ atmosphere (Fig. S26), which is attributed to the limited hydrogen absorption capacity during the hydrogen absorption process at 100 °C. An excellent hydrogenation performance was also obtained by $MgH_2$–ZrTi@10nm$Al_2O_3$ (Fig. 4d). About 2.59 wt% of $H_2$ was absorbed by $MgH_2$–ZrTi@10nm$Al_2O_3$ at 50 °C within 15 min, extending to 3.92 wt% with hydrogenation time prolonged to 2 h. The hydrogenation capacity of $MgH_2$–ZrTi@10nm$Al_2O_3$ was observed to be significantly increased at 75 °C with 3.42 wt% $H_2$ absorbed within 15 min, while 4.44 wt% in 1 h and 4.97 wt% in 3 h. The surge in hydrogenation rate is attributable to the rapid enhancement of the reactivity of $MgH_2$–ZrTi@10nm$Al_2O_3$ upon increasing temperature, analogous to the hydrogenation behavior of the reported blank $MgH_2$–ZrTi [26]. The initial hydrogenation rate was deduced to reach 0.228 wt% $min^{-1}$ at 75 °C based on the first 15 min since the transition point of the curve proportion limit is located at 15 min (Fig. 4d, light green). The hydrogenation curve of $MgH_2$–ZrTi@10nm$Al_2O_3$ at 100 °C was found to reach its inflection point within 5 min with 4.51 wt% $H_2$ absorbed, while absorbing 5.46 wt% of $H_2$ within 1.5 h. The hydrogenation kinetics of $MgH_2$–ZrTi@10nm$Al_2O_3$ at 125 °C (Fig. 4d, red) was found to be similar to that at 100 °C. The $MgH_2$–ZrTi@10nm$Al_2O_3$ has been demonstrated to have rapid hydrogenation capabilities between 75 and 100 °C, which is able to be realized by using solar energy effectively in the future. Both the average hydrogenation rate before the transition point and initial dehydrogenation rate within the first 10 min of $MgH_2$–ZrTi@10nm$Al_2O_3$ have been demonstrated to be much better than reported air-stabilized Mg-based composites under the same data-intercept conditions (Fig. 4e, f) [18–20].

The cycling performance of $MgH_2$–ZrTi@10nm$Al_2O_3$ was also conducted (Fig. 4g). The dehydrogenation capacity of $MgH_2$–ZrTi@10nm$Al_2O_3$ was found to gradually increase from 5.19 to 5.23 wt% during the first 10 cycles due to gradual activation of hydrogen storage material particles during the de/re-hydrogenation cycles. About 5.12 and 5.04 wt% of $H_2$ were detected to release from $MgH_2$–ZrTi@10nm$Al_2O_3$ even after the 20th and 30th cycles, respectively. The dehydrogenation cycling capacity of $MgH_2$–ZrTi@10nm$Al_2O_3$ was found to be stable after 40 cycles (4.96 wt%), where

4.97 wt% was detected after 50 cycles. The re-hydrogenation behavior during cycling was observed to be similar to the trend of dehydrogenation one (Fig. 4g). The re-hydrogenation capacity was detected to increase from 5.30 to 5.42 wt% in the first 10 cycles. The re-hydrogenation capacity was detected to be 5.26, 4.9, 4.96, and 4.96 wt% at the 20th, 30th, 40th and 50th cycle, respectively. Amorphous $Al_2O_3$ shells were observed to be robust on the surface of $MgH_2$ particles even after 50 cycles by HAADF-STEM and corresponding elemental analyses (Fig. 4h), consistent well with the high cycling performance of $MgH_2$–ZrTi@10nm$Al_2O_3$. The $MgH_2$–ZrTi@10nm$Al_2O_3$ has been demonstrated to have excellent cycling performance with a capacity retention of 95.0% after 50 cycles.

### 3.5 Analysis of Hydrogen Sorption Processes for $MgH_2$–ZrTi@10nm$Al_2O_3$

The isothermal dehydrogenation curve of $MgH_2$–ZrTi@10nm$Al_2O_3$ at 275 °C (Figs. 4c, S24a, and S25a) was fitted using a rapid screening method of kinetic models [31, 32] to explore the dehydrogenation kinetic of $MgH_2$–ZrTi@10nm$Al_2O_3$. The R2 (two-dimensional phase boundary) model [33] was found to suit the dehydrogenation kinetic of $MgH_2$–ZrTi@10nm$Al_2O_3$ after re-hydrogenation under pure $H_2$ best since its slope (1.017) is closest to 1 and intercept (−0.0048) closest to 0 among nine kinetic models (Fig. 5a). The kinetic model of $MgH_2$–ZrTi@10nm$Al_2O_3$ after re-hydrogenation in 30 bar 10%$CH_4$ + 90%$H_2$ or 16 bar 0.1%$O_2$ + 0.4%$N_2$ + 99.5%$H_2$ at 100 °C for 1 h was further fitted based on the isothermal dehydrogenation data at 275 °C (Figs. S24a and S25a). The R2 model was also found to be the most suitable one for describing the dehydrogenation behavior of $MgH_2$–ZrTi@10nm$Al_2O_3$ (Figs. S24b and S25b), suggesting no effect was caused by the re-hydrogenation in atmospheres containing $CH_4$, $O_2$, and $N_2$ to the kinetics of $MgH_2$–ZrTi@10nm$Al_2O_3$. Subsequently, the apparent activation energy ($E_a$) for dehydrogenation was fitted based on the isothermal dehydrogenation data for $MgH_2$–ZrTi@10nm$Al_2O_3$ after re-hydrogenation in 30 bar $H_2$ (Fig. 4c). The isothermal dehydrogenation ratios α (at the range of 0–0.7) at different time scales under different temperatures from Fig. 4c were then substituted into the R2 model to obtain g(α)-Time curves (Fig. 5b). All three g(α)-Time curves were observed to have excellent linearity, further confirming the suitability of the R2 model for the dehydrogenation kinetic of $MgH_2$–ZrTi@10nm$Al_2O_3$. The slopes of the g(α)-Time curves as well as the corresponding temperatures were substituted into the Arrhenius equation to calculate the $E_a$ of the dehydrogenation of $MgH_2$–ZrTi@10nm$Al_2O_3$ (Fig. 5c) [34]. The dehydrogenation activation energy $E_a$ of $MgH_2$–ZrTi@10nm$Al_2O_3$ was found to slightly increase to 105.92 kJ $mol^{-1}$ from that of $MgH_2$–ZrTi ($E_a$ = 97.77 kJ $mol^{-1}$) [26], consistent well with the slightly slower dehydrogenation rate of $MgH_2$–ZrTi@10nm$Al_2O_3$ (Fig. 4a, b) than that of $MgH_2$–ZrTi (Fig. S3) due to $Al_2O_3$ coating.

The kinetic of $MgH_2$–ZrTi@10nm$Al_2O_3$ has been demonstrated to follow R2 model where re-hydrogenation under 30 bar $H_2$, 30 bar 10%$CH_4$ + 90%$H_2$, or 16 bar 0.1%$O_2$ + 0.4%$N_2$ + 99.5%$H_2$. The conversion reaction between $MgH_2$ and Mg has been demonstrated to occur rapidly on the surface of $MgH_2$ particles under the synergistic effect of amorphous $ZrO_2$ and FL-$Ti_3C_2$, where effective hydrogen channels were built [26]. The $H_2$ molecules were first diffused through the amorphous $Al_2O_3$ shells, with the $MgH_2$/Mg interfaces formed on the surface of the hydrogen storage particles and moved to the interior of the particles through hydrogen channels at a uniform speed [34]. The movement of the $MgH_2$/Mg interface was determined by the co-catalytic ability of amorphous $ZrO_2$ and FL-$Ti_3C_2$ as well as the penetration rate of $H_2$ molecules through amorphous $Al_2O_3$ shells, which is the key factors for the dehydrogenation kinetic of $MgH_2$–ZrTi@10nm$Al_2O_3$.

The amorphous $Al_2O_3$ shells were clearly observed on the surface of $MgH_2$–ZrTi@10nm$Al_2O_3$ after re/dehydrogenation by TEM as well as HRTEM images (Figs. 5d, e, and S27), consistent well with its robust features to prevent reaction of $MgH_2$–ZrTi with impurities. Only the interplanar spacing of 0.19 nm corresponding to the (102) plane of Mg (JCPDS No. 35-0821) was observed from the HRTEM image of dehydrogenated $MgH_2$–ZrTi@10nm$Al_2O_3$ (Fig. 5e), while only interplanar spacing of 0.25 nm corresponding to the (101) plane of $MgH_2$ (JCPDS No. 12-0697) was observed from re-hydrogenated ones (Fig. S27b). The amorphous $Al_2O_3$ shells (Figs. 5e and S27) were still observed after re/dehydrogenation, further confirming their robust features during re/dehydrogenation. The amorphous feature of $Al_2O_3$ shells is well consistent with its XRD feature (Fig. 5f). The HRTEM images are consistent well with XRD spectra of $MgH_2$–ZrTi@10nm$Al_2O_3$ at different stages, where only

 https://doi.org/10.1007/s40820-025-01934-7

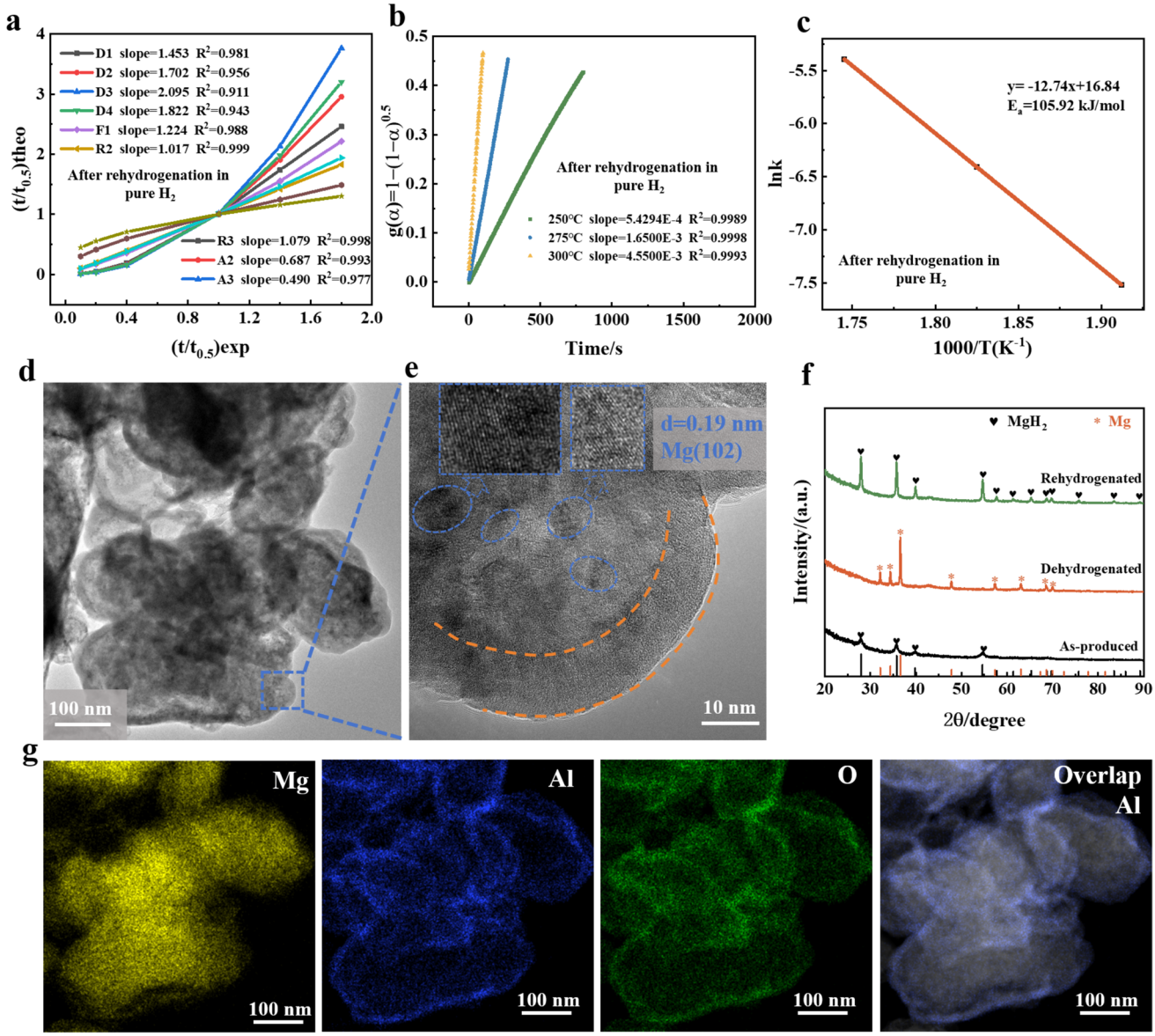


**Fig. 5** **a** Relationships of $(t/t_{0.5})_{theo}$ vs. $(t/t_{0.5})_{exp}$ of $MgH_2$–ZrTi@10nm$Al_2O_3$ at 275 °C according to various kinetic models. **b** Time dependence of R2 modeling equation g(α) for $MgH_2$–ZrTi@10nm$Al_2O_3$ at different temperatures. **c** Arrhenius plot for the dehydrogenation kinetics of $MgH_2$–ZrTi@10nm$Al_2O_3$. **d** TEM, **e** HRTEM, and **g** corresponding elemental mapping analysis of $MgH_2$–ZrTi@10nm$Al_2O_3$ after dehydrogenation. **f** XRD patterns of $MgH_2$–ZrTi@10nm$Al_2O_3$ before and after de/re-hydrogenation

XRD pattern of Mg was observed from the dehydrogenated $MgH_2$–ZrTi@10nm$Al_2O_3$ (Fig. 5f, red line) and only XRD pattern of $MgH_2$ was observed from the re-hydrogenated one (Fig. 5f, green line). No XRD patterns of crystalline $Al_2O_3$ were observed from $MgH_2$–ZrTi@10nm$Al_2O_3$ at any stages, further confirming its amorphous nature without any variation during re/dehydrogenation treatments. Only diffraction peaks corresponding to Mg and $MgH_2$ were detected in the XRD of the de/re-hydrogenated one, indicating no detectable Mg–Al oxides were generated during heat treatments.

The chemical state variation during de/re-hydrogenation was further characterized by X-ray photoelectron spectroscopy (XPS) for $MgH_2$–ZrTi@10nm$Al_2O_3$ in different states (Fig. S28). The signal at 75.9 eV corresponding to amorphous $Al_2O_3$ [35] was detected from the high-resolution Al 2*p* XPS spectrum of the as-produced

$MgH_2$–ZrTi@10nm$Al_2O_3$ (Fig. S28a). However, the Al 2*p* signal of $MgH_2$–ZrTi@10nm$Al_2O_3$ was observed to be shifted to lower energy level by 1.23 to 74.7 eV after de/re-hydrogenation, indicating electron doping of Al after de/re-hydrogenation process. The difference in electronegativity of Al (1.61), Ti (1.54), and Zr (1.33) in $MgH_2$–ZrTi@10nm$Al_2O_3$ resulted in the tendency of Al to attract electrons while Ti and Zr tended to provide electrons. Therefore, the shift in Al 2*p* spin–orbit peaks was attributed to Al-O-Ti and Al-O-Zr bonding between sublayers of $Al_2O_3$, $Ti_3C_2$, and $ZrO_2$ atoms, consistent well with reported studies [35, 36]. The high-resolution Mg 1 *s* signal was only resolved into a single peak at 1303.5 eV (Fig. S28b) [37], where Mg 1 *s* corresponding to $Mg(OH)_2$ (1302.7 eV [38]), MgO (1303.9 eV [39]), and $MgAl_2O_4$ (1304 eV [40]) were found to be negligible. The generation of hydrolysis, oxidation, or Mg–Al-oxides phases has been demonstrated to be negligible during the de/re-hydrogenation process.

The structural stability of $MgH_2$–ZrTi@10nm$Al_2O_3$ during the de/re-hydrogenation was further verified by HAADF-STEM and corresponding elemental analyses (Figs. 5g, S29, and S30). The shell-like structure composed of Al and O elements was still clearly observed on the surface of $MgH_2$–ZrTi@10nm$Al_2O_3$ particles after both dehydrogenation (Fig. 5g) and re-hydrogenation (Fig. S30), further confirming the robustness of $Al_2O_3$ shells. No size variation was observed for $MgH_2$–ZrTi@10nm$Al_2O_3$ particles, indicating no particle melting or growth occurred from dehydrogenation (Fig. S31) or re-hydrogenation (Fig. S32) treatments. The stable structure is particularly conducive to the stable kinetic of $MgH_2$–ZrTi@10nm$Al_2O_3$, consistent well with the excellent cycling performance of $MgH_2$–ZrTi@10nm$Al_2O_3$ (Fig. 4g).

## 4 Conclusion

The atomic layer amorphous $Al_2O_3$ shells have been successfully deposited on the surface of highly active $MgH_2$–ZrTi hydrogen storage material particles to obtain $MgH_2$–ZrTi@$Al_2O_3$ by ALD. The $Al_2O_3$ shells have been demonstrated to be inert and effectively shielding against $H_2O$, $CH_4$, $O_2$, $N_2$, and $CO_2$ while allowing $H_2$ to penetrate easily, thereby achieving excellent air stability and selective hydrogen absorption performance. The dehydrogenation curves of $MgH_2$–ZrTi@10nm$Al_2O_3$ were found to almost overlap before and after air exposure for 1 day, whereas almost no $H_2$ was released from $MgH_2$–ZrTi after exposure to air even at 275 °C. The $MgH_2$–ZrTi@10nm$Al_2O_3$ was found to have excellent de/re-hydrogenation performance, with an onset dehydrogenation temperature as low as 185 °C and an absorption of 5.00 wt% of $H_2$ at 75 °C within 3 h. About 5.00 wt% of $H_2$ was still released from $MgH_2$–ZrTi@10nm$Al_2O_3$ even after 50 cycles, with a capacity retention of up to 95%. The amorphous $Al_2O_3$ was demonstrated to be robust and maintain its shell-like structure after the de/re-hydrogenation, consistent with its high cycling stability. The $MgH_2$–ZrTi@10nm$Al_2O_3$ has also been demonstrated to have high selective hydrogen absorption performance under impure hydrogen. The $MgH_2$–ZrTi@10nm$Al_2O_3$ was demonstrated to have selective hydrogen adsorption in 10%$CH_4$ + 90%$H_2$ atmosphere (absorb 4.79 wt% $H_2$ at 75 °C for 3 h), where no kinetic or density decay was observed after 30 cycles at 100 °C (96.9% capacity retention). However, the $CH_4$ was detected to react with $MgH_2$–ZrTi without $Al_2O_3$ shells to produce amorphous C deposition. $MgH_2$–ZrTi@10nm$Al_2O_3$ has also been demonstrated to have selective hydrogen adsorption in 0.1%$O_2$ + 0.4%$N_2$ + 99.5%$H_2$ atmosphere. About 4.1 wt% of $H_2$ was absorbed by $MgH_2$–ZrTi@10nm$Al_2O_3$ within 1 h at 100 °C, with a capacity retention of up to 89.4% after 20 hydrogen absorption cycles. In contrast, the hydrogen adsorption behavior of $MgH_2$–ZrTi under 0.1%$O_2$ + 0.4%$N_2$ + 99.5%$H_2$ atmosphere decayed rapidly. The $MgH_2$–ZrTi@10nm$Al_2O_3$ have also been demonstrated to have excellent selective hydrogen absorption performance even with extremely high $O_2$ atmosphere by two-step absorption method. The isothermal re/dehydrogenation curves of $MgH_2$–ZrTi@10nm$Al_2O_3$ after hydrogenation in pure $H_2$ followed by 21%$O_2$ + 79%$N_2$ at 75 °C for 1 h were found to overlap with those after hydrogenation in pure $H_2$. In addition, about 4.0 wt% of $H_2$ was absorbed by the $MgH_2$–ZrTi@10nm$Al_2O_3$ at 100 °C within 0.5 h under 0.1%$CO_2$ + 0.4%$N_2$ + 99.5%$H_2$ atmosphere, while the hydrogen absorption behavior of the $MgH_2$–ZrTi was significantly attenuated under the same conditions. The $MgH_2$–ZrTi@10nm$Al_2O_3$ have been demonstrated to have excellent selective hydrogen absorption performance in the presence of different amounts of $CH_4$, $O_2$, $N_2$, and $CO_2$.

**Acknowledgements** The TEM studies were carried out at the Instrument Analysis Center of the Xi'an Jiaotong University. The

 https://doi.org/10.1007/s40820-025-01934-7

authors thank Mr C. Li for his help in using TEM. The research was supported by the National Natural Science Foundation of China (22175136), the State Key Laboratory of Electrical Insulation and Power Equipment (EIPE23127), and the Fundamental Research Funds for the Central Universities (xtr052024009).

**Author Contributions** Fanqi Bu: Conceptualization, Investigation, Methodology, Writing-original draft, Writing-review & editing, Data curation, Zhenyu Wang: Software, Visualization, Ali Wajid: Software, Rui Zhai: Visualization, Ting Liu: Visualization, Yaohua Li: Visualization, Xin Ji: Resources, Xin Liu: Resources, Shujiang Ding: Resources, Yonghong Cheng: Resources, Jinying Zhang: Writing-review & editing, Funding acquisition, Project administration, Supervision.

**Declarations**

**Conflict of interest** The authors declare no interest conflict. They have no known competing financial interests or personal relationships that could have appeared to influence the work reported in this paper.



**Supplementary Information** The online version contains supplementary material available at https://doi.org/10.1007/s40820-025-01934-7.

## References

1. Y. Sun, C. Shen, Q. Lai, W. Liu, D.-W. Wang et al., Tailoring magnesium based materials for hydrogen storage through synthesis: current state of the art. Energy Storage Mater. **10**, 168–198 (2018). https://doi.org/10.1016/j.ensm.2017.01.010
2. M. Chen, X. Xiao, X. Wang, Y. Lu, M. Zhang et al., Self-templated carbon enhancing catalytic effect of $ZrO_2$ nanoparticles on the excellent dehydrogenation kinetics of $MgH_2$. Carbon **166**, 46–55 (2020). https://doi.org/10.1016/j.carbon.2020.05.025
3. C. Gu, H.-G. Gao, P. Tan, Y.-N. Liu, X.-Q. Liu et al., Cheese-like $Ti_3C_2$ for enhanced hydrogen storage. Chem. Eng. J. **473**, 145462 (2023). https://doi.org/10.1016/j.cej.2023.145462
4. J. Mao, T. Huang, S. Panda, J. Zou, W. Ding, Direct observations of diffusion controlled microstructure transition in Mg–In/Mg–Ag ultrafine particles with enhanced hydrogen storage and hydrolysis properties. Chem. Eng. J. **418**, 129301 (2021). https://doi.org/10.1016/j.cej.2021.129301
5. R. Shi, H. Yan, J. Zhang, H. Gao, Y. Zhu et al., Vacancy-mediated hydrogen spillover improving hydrogen storage properties and air stability of metal hydrides. Small **17**(31), 2100852 (2021). https://doi.org/10.1002/smll.202100852
6. W. Zhu, L. Ren, C. Lu, H. Xu, F. Sun et al., Nanoconfined and *in situ* catalyzed $MgH_2$ self-assembled on 3D $Ti_3C_2$ MXene folded nanosheets with enhanced hydrogen sorption performances. ACS Nano **15**(11), 18494–18504 (2021). https://doi.org/10.1021/acsnano.1c08343
7. G. Xia, Y. Tan, X. Chen, D. Sun, Z. Guo et al., Monodisperse magnesium hydride nanoparticles uniformly self-assembled on graphene. Adv. Mater. **27**(39), 5981–5988 (2015). https://doi.org/10.1002/adma.201502005
8. M. Liu, S. Zhao, X. Xiao, M. Chen, C. Sun et al., Novel 1D carbon nanotubes uniformly wrapped nanoscale $MgH_2$ for efficient hydrogen storage cycling performances with extreme high gravimetric and volumetric capacities. Nano Energy **61**, 540–549 (2019). https://doi.org/10.1016/j.nanoen.2019.04.094
9. L. Ren, W. Zhu, Y. Li, X. Lin, H. Xu et al., Oxygen vacancy-rich 2D $TiO_2$ nanosheets: a bridge toward high stability and rapid hydrogen storage kinetics of nano-confined $MgH_2$. Nano-Micro Lett. **14**(1), 144 (2022). https://doi.org/10.1007/s40820-022-00891-9
10. Z. Lan, F. Hong, W. Shi, R. Zhao, R. Li et al., Effect of MOF-derived carbon–nitrogen nanosheets Co-doped with nickel and titanium dioxide nanoparticles on hydrogen storage performance of $MgH_2$. Chem. Eng. J. **468**, 143692 (2023). https://doi.org/10.1016/j.cej.2023.143692
11. L. Zhang, Z. Cai, X. Zhu, Z. Yao, Z. Sun et al., Two-dimensional ZrCo nanosheets as highly effective catalyst for hydrogen storage in $MgH_2$. J. Alloys Compd. **805**, 295–302 (2019). https://doi.org/10.1016/j.jallcom.2019.07.085
12. J. Yang, W. Shi, R. Liu, Y. Tan, Y. Fan et al., MXene-supported $V_2O_5$ nanocatalysts: boosting hydrogen storage efficiency in $MgH_2$ through synergistic catalysis. J. Energy Storage **130**, 117474 (2025). https://doi.org/10.1016/j.est.2025.117474
13. Z. Yang, J. Wu, Y. Wang, S. Wang, Y. Zou et al., Improved hydrogen storage performance of magnesium hydride catalyzed by two dimensional $Ti_3C_2$-coated NbN. J. Alloys Compd. **1029**, 180752 (2025). https://doi.org/10.1016/j.jallcom.2025.180752
14. K.C. Tome, S. Xi, Y. Fu, C. Lu, N. Lu et al., Remarkable catalytic effect of Ni and $ZrO_2$ nanoparticles on the hydrogen sorption properties of $MgH_2$. Int. J. Hydrog. Energy **47**(7), 4716–4724 (2022). https://doi.org/10.1016/j.ijhydene.2021.11.102
15. X. Zhang, Y. Sun, S. Ju, J. Ye, X. Hu et al., Solar-driven reversible hydrogen storage. Adv. Mater. **35**(2), e2206946 (2023). https://doi.org/10.1002/adma.202206946
16. X. Hu, X. Chen, X. Zhang, Y. Meng, G. Xia et al., *In situ* construction of interface with photothermal and mutual catalytic effect for efficient solar-driven reversible hydrogen storage of

$MgH_2$. Adv. Sci. **11**(22), 2400274 (2024). https://doi.org/10.1002/advs.202400274

17. Y. Jiang, Y. Sun, Y. Liu, M. Yue, Y. Cao et al., Solar-driven reversible hydrogen storage in metal oxides-catalyzed $MgH_2$. Int. J. Hydrogen Energy **149**, 150101 (2025). https://doi.org/10.1016/j.ijhydene.2025.150101
18. M. Chen, X. Xie, P. Liu, T. Liu, Facile fabrication of ultrathin carbon layer encapsulated air-stable Mg nanoparticles with enhanced hydrogen storage properties. Chem. Eng. J. **337**, 161–168 (2018). https://doi.org/10.1016/j.cej.2017.12.087
19. K.-J. Jeon, H.R. Moon, A.M. Ruminski, B. Jiang, C. Kisielowski et al., Air-stable magnesium nanocomposites provide rapid and high-capacity hydrogen storage without using heavy-metal catalysts. Nat. Mater. **10**(4), 286–290 (2011). https://doi.org/10.1038/nmat2978
20. W. Ali, Y. Qin, N.A. Khan, H. Zhao, Y. Su et al., Highly air-stable magnesium hydrides encapsulated by nitrogen-doped graphene nanospheres with favorable hydrogen storage kinetics. Chem. Eng. J. **480**, 148163 (2024). https://doi.org/10.1016/j.cej.2023.148163
21. Z. Ma, Q. Tang, J. Ni, Y. Zhu, Y. Zhang et al., Synergistic effect of $TiH_2$ and air exposure on enhancing hydrogen storage performance of $Mg_2NiH_4$. Chem. Eng. J. **433**, 134489 (2022). https://doi.org/10.1016/j.cej.2021.134489
22. J. Zhang, W. Wang, X. Chen, J. Jin, X. Yan et al., Single-atom Ni supported on $TiO_2$ for catalyzing hydrogen storage in $MgH_2$. J. Am. Chem. Soc. **146**(15), 10432–10442 (2024). https://doi.org/10.1021/jacs.3c13970
23. J. Xu, W. Lin, Integrated hydrogen liquefaction processes with LNG production by two-stage helium reverse Brayton cycles taking industrial by-products as feedstock gas. Energy **227**, 120443 (2021). https://doi.org/10.1016/j.energy.2021.120443
24. Y. Zhang, Q. Li, P. Shen, Y. Liu, Z. Yang et al., Hydrogen amplification of coke oven gas by reforming of methane in a ceramic membrane reactor. Int. J. Hydrog. Energy **33**(13), 3311–3319 (2008). https://doi.org/10.1016/j.ijhydene.2008.04.015
25. Y.J. Kwak, M.Y. Song, K.-T. Lee, Conversion of $CH_4$ and hydrogen storage *via* reactions with $MgH_2$–12Ni. Micromachines **14**(9), 1777 (2023). https://doi.org/10.3390/mi14091777
26. F. Bu, A. Wajid, M. Gu, T. Liu, S. Liu et al., Synergistic effect of multivalent Ti, Zr, and oxygen vacancies to significantly enhance the hydrogen sorption properties of $MgH_2$. J. Mater. Chem. A **13**(21), 16102–16111 (2025). https://doi.org/10.1039/d5ta01302j
27. D. Ma, Z. Wang, J.-W. Shi, Y. Zou, Y. Lv et al., An ultrathin $Al_2O_3$ bridging layer between CdS and ZnO boosts photocatalytic hydrogen production. J. Mater. Chem. A **8**(21), 11031–11042 (2020). https://doi.org/10.1039/D0TA03933K
28. F. Bu, A. Wajid, N. Yang, M. Gu, X. Zhao et al., Fabrication of amorphous $TiO_2$ hydrogen channels and graphene wrappers to enhance the hydrogen storage properties of $MgH_2$ with extremely high cycle stability. J. Mater. Chem. A **12**(20), 12190–12197 (2024). https://doi.org/10.1039/D4TA00722K
29. N. Grønbech-Jensen, O. Farago, A simple and effective Verlet-type algorithm for simulating Langevin dynamics. Mol. Phys. **111**(8), 983–991 (2013). https://doi.org/10.1080/00268976.2012.760055
30. L. Tian, H. Duan, J. Luo, Y. Cheng, L. Shi, Density functional theory and molecular dynamics simulations of nanoporous graphene membranes for hydrogen separation. ACS Appl. Nano Mater. **4**(9), 9440–9448 (2021). https://doi.org/10.1021/acsanm.1c01919
31. J.H. Sharp, G.W. Brindley, B.N. Narahari Achar, Numerical data for some commonly used solid state reaction equations. J. Am. Ceram. Soc. **49**(7), 379–382 (1966). https://doi.org/10.1111/j.1151-2916.1966.tb13289.x
32. A. Khawam, D.R. Flanagan, Solid-state kinetic models: basics and mathematical fundamentals. ChemInform **37**(47), 200647223 (2006). https://doi.org/10.1002/chin.200647223
33. L.F. Jones, D. Dollimore, T. Nicklin, Comparison of experimental kinetic decomposition data with master data using a linear plot method. Thermochim. Acta **13**(2), 240–245 (1975). https://doi.org/10.1016/0040-6031(75)80085-2
34. H.E. Kissinger, Reaction kinetics in differential thermal analysis. Anal. Chem. **29**(11), 1702–1706 (1957). https://doi.org/10.1021/ac60131a045
35. J. Meyer, H. Schmidt, W. Kowalsky, T. Riedl, A. Kahn, The origin of low water vapor transmission rates through $Al_2O_3$/$ZrO_2$ nanolaminate gas-diffusion barriers grown by atomic layer deposition. Appl. Phys. Lett. **96**(24), 243308 (2010). https://doi.org/10.1063/1.3455324
36. L.H. Kim, K. Kim, S. Park, Y.J. Jeong, H. Kim et al., $Al_2O_3$/$TiO_2$ nanolaminate thin film encapsulation for organic thin film transistors *via* plasma-enhanced atomic layer deposition. ACS Appl. Mater. Interfaces **6**(9), 6731–6738 (2014). https://doi.org/10.1021/am500458d
37. J.C. Fuggle, L.M. Watson, D.J. Fabian, S. Affrossman, X-ray excited Auger and photoelectron spectra of magnesium, some alloys of magnesium and its oxide. J. Phys. F Met. Phys. **5**(2), 375 (1975). https://doi.org/10.1088/0305-4608/5/2/020
38. D.E. Haycock, M. Kasrai, C.J. Nicholls, D.S. Urch, The electronic structure of magnesium hydroxide (brucite) using X-ray emission, X-ray photoelectron, and auger spectroscopy. J. Chem. Soc. Dalton Trans. **12**, 1791–1796 (1978). https://doi.org/10.1039/DT9780001791
39. H. Seyama, M. Soma, X-ray photoelectron spectroscopic study of montmorillonite containing exchangeable divalent cations. J. Chem. Soc., Faraday Trans. 1 **80**(1), 237 (1984). https://doi.org/10.1039/f19848000237
40. D.E. Haycock, C.J. Nicholls, D.S. Urch, M.J. Webber, G. Wiech, The electronic structure of magnesium dialuminium tetraoxide (spinel) using X-ray emission and X-ray photoelectron spectroscopies. J. Chem. Soc. Dalton Trans. **12**, 1785–1790 (1978). https://doi.org/10.1039/DT9780001785